

Scansorial Landing and Perching

Alexis Lussier Desbiens, Alan T. Asbeck, and Mark R. Cutkosky

We describe an approach whereby small unmanned aircraft can land and perch on outdoor walls. Our prototype uses an ultrasonic sensor to initiate a pitch-up maneuver as it flies toward a wall. As it begins to stall, it contacts the wall with compliant “feet” equipped with rows of miniature spines that engage asperities on the surface. A nonlinear hierarchical suspension absorbs the kinetic energy and controls contact forces in the normal and tangential directions to keep spines engaged during the landing process. Future work will include powered take-offs and maneuvering in contact with the wall.

1 Introduction

The work described in this paper is a first step toward small flying robots that can land, maneuver and take off from arbitrary surfaces. Such robots combine the best attributes of climbing robots and unmanned air vehicles (UAVs). They can reach remote sites rapidly, flying directly to them. After landing, they can remain fixed or crawl slowly, while consuming little power. The applications include surveillance, environmental monitoring, and inspection of hard-to reach surfaces on buildings, dams, bridges and other large structures. If the robots cling tenaciously, they can also ride out weather that is too rough for flight. When conditions improve, or when their mission is completed, they can jump off and become airborne again.

We are particularly interested in hybrid *scansorial* robots that are adapted for landing and ultimately maneuvering on arbitrary surfaces such as the walls of buildings. As fig. 1 (right) reveals, in the aftermath of an earthquake or other disaster, horizontal surfaces may be too littered with debris and too dangerous for landing, while vertical surfaces are comparatively unobstructed. Moreover, if the flying robots can take shelter under the eaves of a building (like swallows or bats) they may perch safely and unobtrusively for long periods of time.

Stanford University; Biomimetic and Dextrous Manipulation Laboratory; Center for Design Research; 424 Panama Mall, Bldg. 560; Stanford, CA 94305-2232; e-mail: {alexisld, aasbeck, cutkosky}@stanford.edu

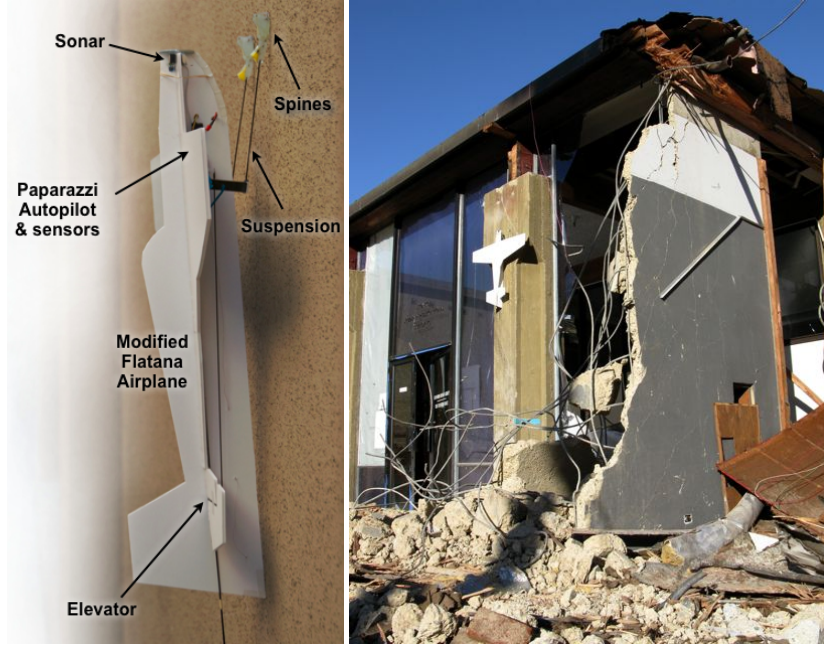


Fig. 1 Left: Our scansorial UAV is based on a modified Flatana (Great Planes, 2009) aerobatic plane. To enable landing on vertical surfaces, several components were added: a controller based on the Paparazzi (Paparazzi, 2008) open-source autopilot, an ultrasonic range sensor, a nonlinear leg suspension and compliant ankles and toes equipped with miniature spines. The fully loaded airplane has a mass of 400g, the landing system accounting for only 28g. Right: Sometimes the best place to land is a wall.

The development of scansorial flying robots draws directly upon two areas of work: unmanned air vehicles capable of acrobatic maneuvers, and vertical climbing robots. In the following section we briefly review the relevant prior work in each of these areas. We then present our approach, which utilizes a small fixed-wing airplane based on the popular Flatana (Great Planes, 2009) platform, as shown in fig. 1 (left). The plane uses feet equipped with miniature spines to grip asperities on the surface. In Section 3 we show that the characteristics of the spines impose constraints on the normal and tangential forces between the plane and the wall. We describe a nonlinear leg suspension in Section 4 that absorbs the kinetic energy of the plane and redirects it toward the feet to satisfy the spine/wall interaction constraints.

The problem of increasing the reliability of scansorial perching has two parts: the first is to design a suspension that will achieve spine engagement and loading for as wide a range of initial contact orientations and velocities as possible; the second is to control the plane so that it reliably approaches the wall within a given envelope of velocities and orientations, despite gusts of wind, etc. In this paper we focus on the former problem using a combination of modeling and experiments with an unpowered glider and a wall with a force plate. We conclude with a discussion

of ongoing work to increase the reliability of the approach in outdoor conditions and future work to permit maneuvering on the wall and powered take-off to resume flight.

1.1 Previous Work

Prior related work includes unmanned air vehicles that can perform aerobatic maneuvers such as hovering and alighting on structures. In one approach, researchers (Frank et al, 2007) have used motion capture cameras to control an RC plane for maneuvers such as flying in a room and hovering to land on a docking station. A similar system was used in (Cory and Tedrake, 2008) to create an accurate high-dimensional model of a glider during high angle-of-attack (AOA) maneuvers required during perching. Using this model, they show (Roberts et al, 2009) that the glider becomes less controllable as its airspeed drops just before perching, even if controllability is improved with a fixed propeller or thrust vectoring. Newer work has focused on simplifying the high-dimensional model in a form suitable for the design of feedback controllers (Hoburg and Tedrake, 2009) and on sensors for the detection of electrical wires (Moore and Tedrake, 2009). In other work, autonomous hovering has been demonstrated with fixed-wing aircraft (Green and Oh, 2008). Still other work has focused on performing perching maneuvers using a morphing airplane (Wickenheiser and Garcia, 2008) to maintain controllability.

Recent work at the Air Force Research Laboratory has investigated the aerodynamics and power requirements for a mechanized wing concept (Reich et al, 2009; Lukens et al, 2008) with application to low-speed maneuvers. Another group has recently investigated several creative solutions for perching UAVs (Anderson et al, 2009). Their most successful approach was to fly directly into a wall with a sticky pad located on the nose. After impact, the aircraft is released and hangs from a tether, which can be cut to take off again.

In much of the previous work, an off-board camera system provides accurate trajectory information along with off-board computation for the controller. For our approach, we are interested in landing repeatedly on outdoor surfaces, without access to external vision data or off-board computing. Fortunately, the accuracy requirements for landing on a wall are less severe than those for perching on a wire or pole. In (Lussier-Desbiens and Cutkosky, 2009) we describe a simple on-board controller and ultrasonic sensor used with our plane. In this paper we focus on the design of the spines and suspension system to accommodate a relatively wide range of initial conditions at first contact.

The second general area of related work is climbing robots. In particular, the work presented here draws directly upon previous results for robots that climb vertical surfaces such as brick, stucco and concrete using arrays of small spines (Asbeck et al, 2006; Spenko et al, 2008). In the future, it may also be possible to adapt directional dry adhesion (e.g. as used by Kim et al (2008)) for perching aircraft.

Extensive biological research has also been devoted to flying and to ground locomotion. However, much less has focused on the physics of transitions that occur

during perching. It has been suggested that flying evolved from the advantages of having even a small amount of lift to control and reduce landing forces (Caple et al, 1983). An example of this phenomenon can be found in the flying squirrel, with its low aspect ratio wing providing aerodynamic stability and lift at angles of attack up to 40 degrees. Furthermore, squirrels deliberately stall themselves prior to landing, allowing them to reduce by 60% their horizontal velocity, while spreading the impact over all four limbs (Byrnes et al, 2008; Paskins et al, 2007). Animals such as geckos also exploit aerodynamics for gliding and landing on vertical surfaces (Jusufi et al, 2008).

2 Dynamic Perching Approach

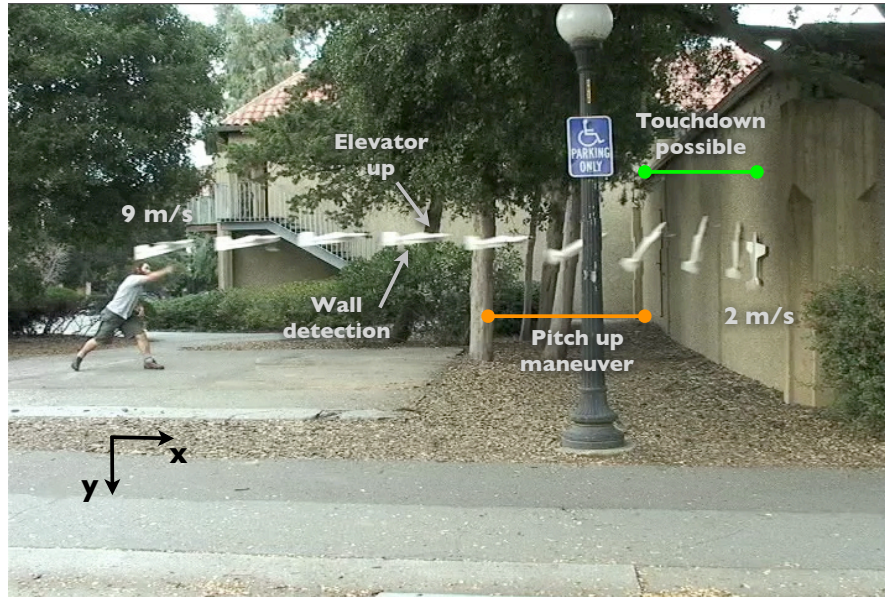


Fig. 2 Landing sequence for dynamic scansorial perching: ultrasonic sensor initiates tilt up at ≈ 5 m from wall; subsequent motion is largely ballistic. Plane contacts wall at 1-3 m/s. Leg and foot suspensions keep spines engaged while dissipating energy.

The basic sequence of landing on a wall is shown in fig. 2. The plane (here an unpowered glider) approaches the wall head-on. When the filtered signal from an onboard ultrasonic sensor indicates that the wall is approximately 5 m away, the plane initiates a pitch-up maneuver to shed speed and align with the wall. Once the plane is nose-up, it starts to fall. The motion of the fixed wing plane after tilt-up is essentially ballistic, with little opportunity for aerodynamic control. As it contacts the wall, the plane is moving with a total velocity of 1-3 m/s. The plane's “feet” con-

tact the wall and drag briefly until the spines engage. Meanwhile, the leg suspension absorbs the kinetic energy of the plane, preventing it from bouncing off the wall or pitching uncontrollably. As described in the next section, for the spines to engage asperities and remain attached, it is important to maintain the normal/tangential force ratio within a certain range throughout the landing. The complete maneuver, from detection to steady perch on the wall, lasts less than one second.

3 Spines

Spines and spine/surface interactions are described in (Asbeck et al, 2006) with application to climbing robots. The spines used here are similar to those used on the RiSE robot (Spenko et al, 2008), but many fewer are needed because the plane is lighter (400g vs. 3.8kg) and keeps both feet in contact throughout the landing. Each foot is equipped with 5 spines consisting of a small hardened steel hooks ($\approx 10 - 25\mu\text{m}$ tip radius) embedded in a molded structure of hard and soft urethane created using Shape Deposition Manufacturing (Cham et al, 2002). The system can be modeled as a damped, elastic linkage as shown in fig. 3.

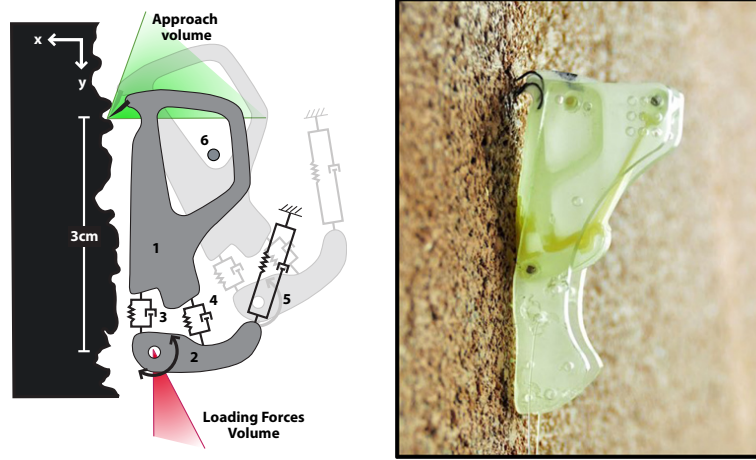


Fig. 3 Left: Model of spine linkage. The spring elements 3 & 4 contribute to the tangential compliance ($k=184\text{ N/m}$ for 3 & 4 in parallel, $\zeta=0.03$), while element 5 provides compliance normal to the wall ($k=16\text{ N/m}$). Element 6, a pin going through the entire foot, acts as an overload protection mechanism in conjunction with the hole in element 1. The approach volume is mostly a function of the shape and orientation of asperities; the loading forces volume also depends on the coefficient of friction. Right: Picture of the spines on the aircraft ankle.

To determine the forces required to engage the spines and keep them attached to the surface, an array of 10 spines was tested on a mechanized stage and force plate previously used for directional adhesion tests (Santos et al, 2007). The stage has a positioning accuracy of $\pm 20\mu\text{m}$ and force measurement accuracy of 25mN .

The spines were tested using a sample of roofing tarpaper, chosen because it has a similar roughness to stucco and is easy to cut to size.

The spines require only small forces to engage, up to a maximum of 0.2 N at the maximum preload deflection of 6.5 mm. The maximum preload deflection is determined by an overload mechanism included in the spine design. As shown in fig. 3, a pin passes through the trapezoidal hole in element 1, limiting its travel and preventing over-stretching of the urethane flexures.

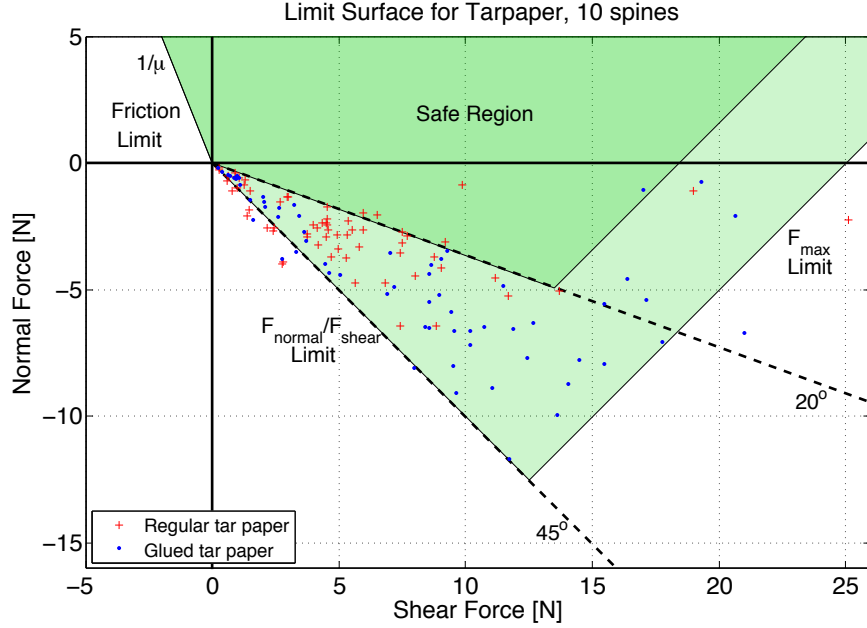


Fig. 4 Limit surface as spines are dragged over unreinforced (red +) and reinforced (blue dots) roofing paper covered with small rock particles. Dark region shows combinations of normal and tangential force that sustain contact without failure; light shaded region shows combinations with occasional failures. When normal force is positive and shear force is negative, Coulomb friction applies.

As the spines drag across the test surface, they can disengage for any of the following reasons:

- they slide off asperities because the loading angle exceeds the F_{normal}/F_{shear} limit for a given spine/asperity contact (Asbeck et al, 2006);
- the asperities dislodge from the surface;
- the spines hit their overload protection pins and detach.

The resulting maximum forces are plotted in fig. 4 as red plus symbols. The normal forces, F_n , are negative, indicating that we are pulling away from the surface ($-x$ direction) and the shear forces, F_s , are positive, indicating that we are pulling in the

positive y direction. If we push the spines in the opposite direction, Coulomb friction applies. We also conducted a second set of tests in which the tarpaper surface was strengthened with a thin layer of cyanoacrylate glue to bond the rock particles more firmly in place. The results of these tests, shown as blue dots, reveal the same trend but with higher average forces.

The general picture that emerges from fig. 4 is that there is a region of normal and shear forces for which the spines attach to the surface without failures. The dark green region, bounded by a 20° line, shows regions where very few failures occurred, whereas occasional failures occurred in the lighter green region bounded by a 45° line corresponding to $-F_n = F_s$. The uncertainty in when a failure will occur is due to the probabilistic nature of the spine-surface interaction: asperities are distributed randomly over the surface, and the maximum loading angle that each asperity can sustain is also a random variable, depending on its shape and local friction conditions. With a population of ten spines, the overall forces are typically due to several spine/asperity contacts in slightly different locations. In theory one could observe trials in which all ten spines did not sustain attachment. However, because the spines are dragged a relatively long distance over the surface (16 mm), this is unlikely. Other constraints on the spine forces arise from the overload mechanism, which limits the overall combination of $-F_n$ and F_s (plotted as F_{max} in fig. 4).

Different surfaces will have different safe regions depending on which failure mechanisms dominate. However, the behavior seen in fig. 4 remains. For surfaces such as rough concrete, the limit corresponding to the spine overload-protection mechanism, which permits a maximum force of ≈ 2 N per spine with a corresponding elastic deflection of ≈ 11 mm, may be the limiting factor. In all cases, the maximum adhesion that can be sustained is a function of the shear force. This relationship has consequences for resisting disturbances such as large gusts of wind and is revisited in section 5. Note also that exceeding the force constraints in fig. 4 is not necessarily catastrophic. If the friction limit for an individual spine/asperity contact is exceeded, or if a particular asperity comes loose, that spine will slip and may reattach, provided that the foot remains in intimate proximity to the wall.

In addition to providing adhesion to the wall, the spines also act as part of the airplane's suspension in series with the leg structure described in section 4. The parallel combination of elements 3 and 4 in fig. 3 has a spring constant of 184 N/m per spine and a damping ratio of $\zeta=0.03$. This low damping ratio causes the plane to rebound upward slightly after the spines are initially loaded. Higher damping in the spine mechanism would be desirable to suppress this effect.

4 Suspension

In contrast to climbing robots, which have control over the force/motion trajectories of their legs, a fixed-wing airplane is essentially ballistic after it has stalled. It is the job of the leg suspension to absorb the kinetic energy of the plane and direct forces to the feet so as to satisfy the constraints depicted in fig. 4. In addition, there are geometric constraints. For example, if the plane and its legs are modeled as a mechanism, only the distal element (i.e., the feet) should contact the wall to avoid

unpredictable forces during landing. Ideally, we wish for these force and kinematic constraints to be satisfied for a wide range of touchdown velocities and pitch angles, so that the requirements on the plane's wall sensor and controller can be reduced and the overall system made simpler and more robust.

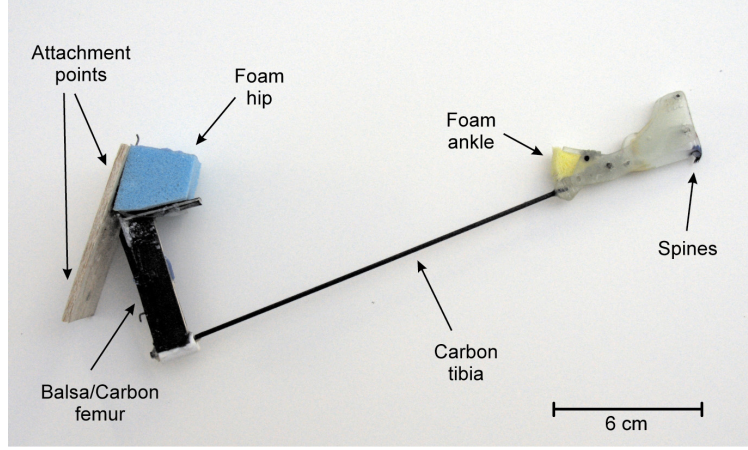


Fig. 5 Compliant leg suspension with stiffness and damping at the hip, knee and ankle.

4.1 Suspension construction

Before going into the details of the modeling, it is useful to describe the suspension. As seen in fig. 5, the suspension has three articulations: the hip, the knee and the ankle. The hip and the ankle are surrounded by urethane foam, providing stiffness and a high level of damping to these joints. Although the tibia (between the knee and ankle) is a carbon fiber strut, it bends enough that we must consider its stiffness when modeling the system.

The hip joint is designed to have a limited range of motion, achieved by placing the foam in compression, in order to protect the propeller of a powered version of the airplane. This construction results in a nonlinear joint stiffness, as shown in fig. 6, which can be approximated by:

$$k_h = 0.0041 + \frac{0.05}{q_h \text{ deg} - 100} \text{ Nm/deg} \quad (1)$$

Damping at the hip is 0.022 Nms/deg for $\theta \geq 130$ deg. and is assumed to scale as $\sqrt{k_h}$ for smaller angles to keep the damping ratio constant.

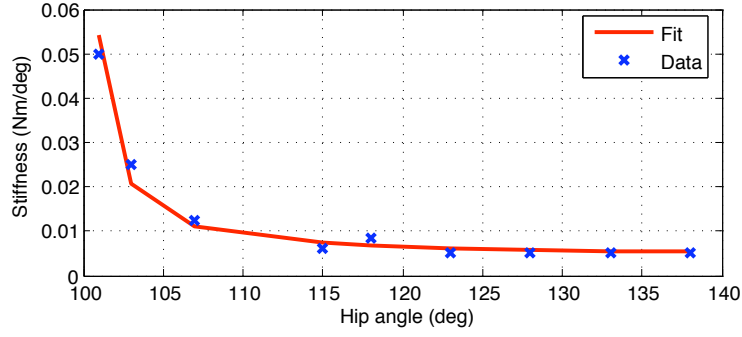


Fig. 6 Hip joint stiffness as a function of the hip angle. The non-linearity prevents excessive compression for high landing forces.

4.2 Planar landing model

In order to predict and tune the forces during landing, a simple planar model of the airplane and suspension was created as shown in fig. 7. In this model we ignore roll and yaw motions and lump the two legs together as a single mechanism. The plane is modeled as a rigid body subject to gravity. We ignore aerodynamic forces as we have determined that they do not contribute significantly to the motion of our plane after contact.

We introduce four right-handed reference frames: The wall frame W is defined with the unit vector \mathbf{w}_x oriented toward the wall and \mathbf{w}_y upward along the surface; the airplane frame A is rotated by θ from W around \mathbf{w}_z , with its origin at the airplane center of mass; the femur frame F is rotated by $-q_H$ from A with its origin at the hip joint; and the tibia frame T , is rotated by q_K from F with its origin at the knee joint.

Intermittent contact forces, \mathbf{N} , with the wall are modeled at the knee and the tail by the use of a spring and damper:

$$\mathbf{N} = \begin{cases} \mathbf{0} & \text{if } x_c < 0 \\ k_g x_c \mathbf{w}_x & \text{if } x_c > 0 \text{ and } \dot{x}_c < 0 \\ (k_g x_c + b_g \dot{x}_c) \mathbf{w}_x & \text{if } x_c > 0 \text{ and } \dot{x}_c > 0 \end{cases} \quad (2)$$

where k_g and b_g are the properties of the ground and $x_c = x_{tail} - x_{wall}$ for the tail point.

Friction at the contact points is modeled using the continuous model from (Mitiguy and Banerjee, 1999):

$$\mathbf{F}_f = -\mu_k |\mathbf{N}| \frac{\mathbf{v}}{|\mathbf{v}| + \epsilon_v} \quad (3)$$

where μ_k is the coefficient of kinetic friction, $|\mathbf{N}|$ is the magnitude of the normal force, \mathbf{v} is the velocity of the point in contact and ϵ_v is a small positive number.

Because of its light weight compared to the airplane, the suspension is modeled as three massless links, ignoring the ankle joint because of its small motion in com-

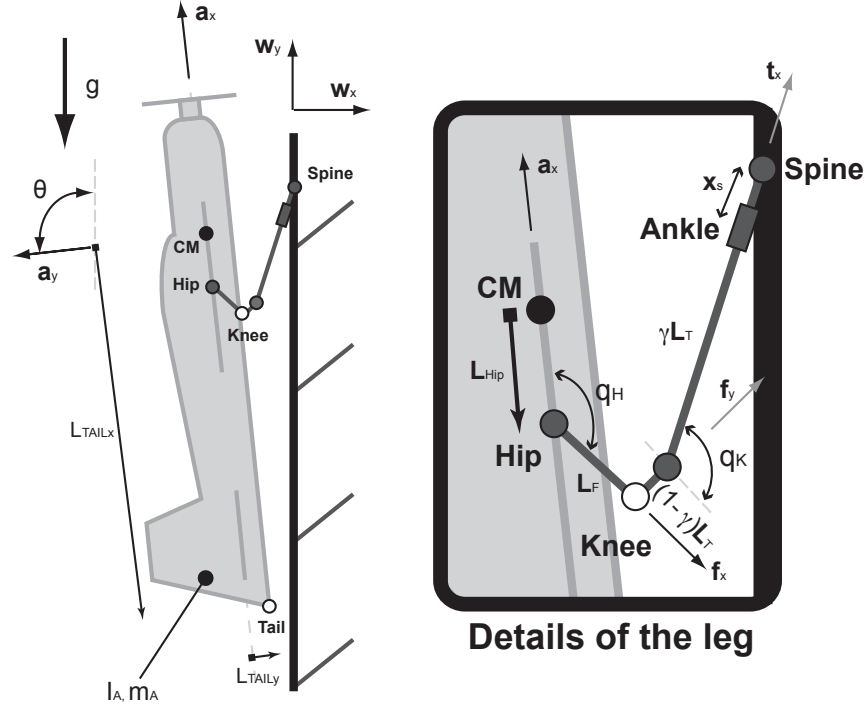


Fig. 7 Planar model: The airplane is a rigid body with possible contacts at the foot, knee and tail. The suspension is a massless linkage with a spring and damper at the hip, knee and spine joints. The knee uses a pseudo-rigid-body approximation (Howell, 2001) to account for large elastic deflection in the tibia.

parison to the femur, tibia and spines. The hip joint is modeled with a non-linear spring and damper as defined in section 4.1, while the spine suspensions are modeled as a prismatic joint with a linear spring as described in section 3.

The large deflection of the tibia can be approximated with a pseudo-rigid-body model of a cantilever beam with a force at the free end (Howell, 2001). This approximation places a pseudo joint at a distance γL from the free end, where L is the length of the tibia and $\gamma \approx 0.85$. The stiffness of the virtual joint can then be expressed as $k_k \approx \pi \gamma^2 EI / L = 0.062 \text{ Nm/deg}$.

Upon contact of the foot with the wall, the linkage of the suspension defines a constraint on the motion of the center of mass of the airplane given by:

$$x \mathbf{w}_x + y \mathbf{w}_y = L_{hip} \mathbf{a}_x - L_f \mathbf{f}_x - (1 - \gamma) L_t \mathbf{f}_y - (\gamma L_t + x_s) \mathbf{t}_x + x_{foot} \mathbf{w}_x + y_{foot} \mathbf{w}_y \quad (4)$$

where \mathbf{w}_x , \mathbf{w}_y , \mathbf{a}_x , \mathbf{f}_x , \mathbf{f}_y and \mathbf{t}_y are unit vectors as defined in fig. 7.

Taking the dot product of this equation with \mathbf{w}_x and \mathbf{w}_y , we obtain two scalar constraint equations that can be differentiated to establish two velocity constraint

relations among the joint angle velocities, \dot{q}_h , \dot{q}_k and \dot{x}_x and the airplane center of mass velocity and pitch rate:

$$\begin{bmatrix} \dot{x}_{foot} \\ \dot{y}_{foot} \end{bmatrix} = J \begin{bmatrix} \dot{q}_h \\ \dot{q}_k \\ \dot{x}_s \end{bmatrix} + f(\dot{x}, \dot{y}, \dot{\theta}) \quad (5)$$

where the \dot{x}_{foot} and \dot{y}_{foot} are zero because we assumed a non-sliding contact with the wall. As the linkage is redundant, the preceding equation is not sufficient to solve for the joint velocities given the airplane velocities. However, static equilibrium must be maintained, as the linkage is massless, and this condition can be formulated as:

$$(I - J^T J^{T\#}) \tau = 0 \quad (6)$$

where $J^{T\#}$ is the pseudo-inverse of J^T , and τ is a matrix of joint torques expressed as $-K(q - q_0) - C\dot{q}$. In the case of the linkage presented here, equation 6 gives us three redundant equations, from which one of them can be used in conjunction with equation 5 to solve for the joint velocities.

From the joints positions and velocities, it is possible to compute the torques at each joint. Then, as the joint motions have been computed while being subject to the constraints of the Jacobian matrix, it is possible to discard one column of the Jacobian matrix to obtain a reduced version (J_r^T) that can be inverted to find the tip forces at the end of the foot:

$$\begin{bmatrix} F_{foot_x} \\ F_{foot_y} \end{bmatrix} = J_r^{T^{-1}} \begin{bmatrix} \tau_{hip} \\ \tau_{knee} \end{bmatrix} \quad (7)$$

With gravity, tail contact and foot forces established, the equations of motion are generated with AutolevTM, an analytical motion analysis software program, which also generates the MatlabTM code necessary to solve them.

4.3 Selection of joint parameters

With the model established in the previous section, and for a given suspension geometry and landing state, it is possible to determine the joint parameters that will let the plane land successfully. The success criteria are taken from section 3 for tarpaper, requiring that $-F_n/F_s < 1$, with a maximum total force of 25 N and a landing in which the suspension does not bottom out, so that only the foot contacts the wall.

The construction of the knee provides only a few discrete options for adjusting the overall stiffness and damping. Therefore, most of the tuning is done at the hip. Fixing the knee stiffness at 0.062 Nm/deg and ignoring the knee damping, which has only a small effect in comparison to the hip, a series of landings were simulated for a typical set of initial conditions: $v_x = 1.2$ m/s, $v_y = -0.5$ m/s and $\theta = 97$ deg. As seen in fig. 8 there is a relatively narrow band of possible hip stiffness and damping values around the nominal values given by equation 1 and scaling the damping as described in section 4.1.

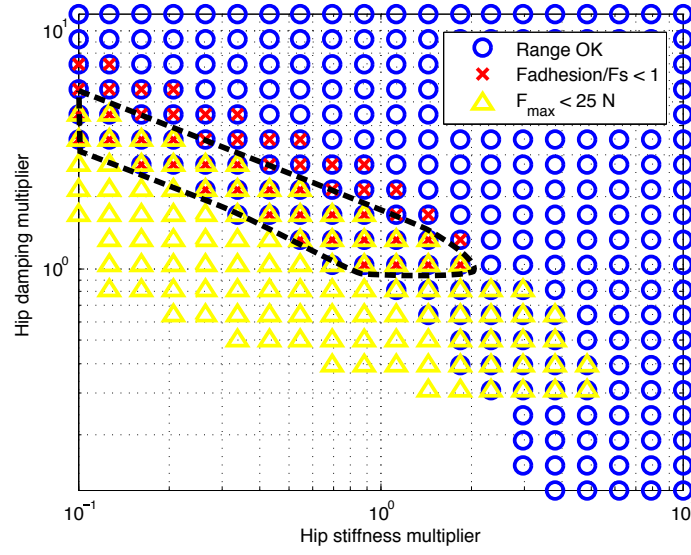


Fig. 8 Successful landings for variations in hip stiffness and damping with respect to the nominal values given by eq. 1. Only a narrow band of combinations satisfies simultaneous constraints on the $-F_n/F_s$ ratio, the maximum force, F_{max} , and acceptable ranges of joint motion for typical landing velocities, $v_x = 1.2$ m/s and $v_y = -0.5$ m/s.

4.4 Experimental validation

To validate our model, the plane was landed on an instrumented wall. The instrumented wall consists of an ATI-Gamma SI-32-2.5 force sensor installed behind a 30x30cm piece of wall material. The force plate has a natural frequency of 100 Hz in the shear direction and 130 Hz in the normal direction. Forces were filtered using a 75Hz Butterworth filter for both the data and the simulation. The touchdown velocity and pitch angle were obtained by analyzing a 30 fps video of the landing.

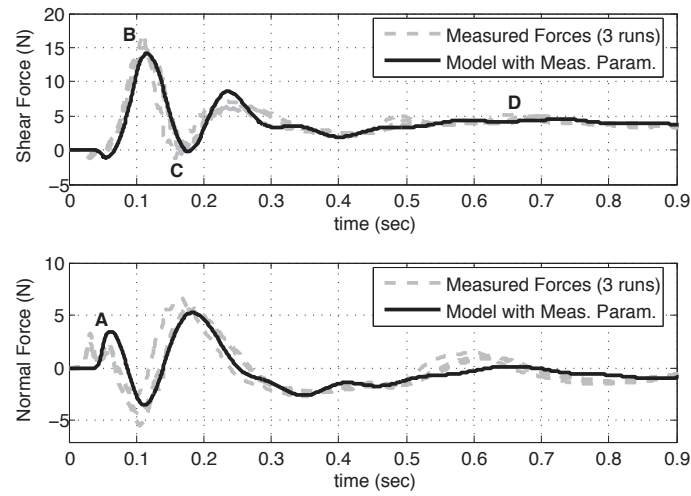


Fig. 9 Comparison between measured and simulated forces. Point **A** represents the touchdown (one impact for each foot in the real data). The shear force then peaks at point **B** when the tail touches the wall, and reaches equilibrium at point **D**. The dip in shear forces at point **C** represents the springback force due to the spine suspension.

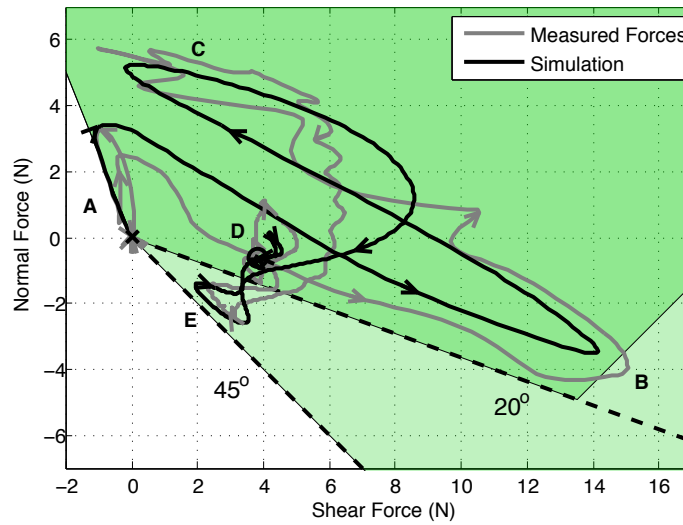


Fig. 10 Comparison of typical measured and simulated force trajectories plotted with respect to the safe regions given by fig. 4. The forces initially pass through point **A** as the tail of the plane touches the wall. The shear force then increases to **B**. The spines are then unloaded by their suspensions at **C** and reach a steady-state value at **D**. The critical point is at **E**, the point of maximum rebound.

Figures 9 and 10 compare typical results between the data collected on the force plate and the one generated with our simulator. To match the measured data, the joint stiffness and damping in the simulation were tuned using a genetic algorithm and resulted in a best-fit joint stiffness approximately 60% higher than what was measured during static tests. The values for the ground parameters in the simulation were roughly guessed, as they have a limited influence on the system response which is dominated by the soft suspension.

Figure 10 shows more specifically that the forces remain, during the landing, in the safe 45° region for reinforced tarpaper as defined in fig. 4. The critical state is at point **E**, as the plane rebounds immediately after the initial impact. Increasing damping would reduce the rebound and increase the safety margin, progressing from **C** to point **D**. The main difference between the simulator and the measured forces, as shown in fig. 9 at point **A**, is that we can observe on the real data the impact of each foot while our model lumps both feet together.

The resulting spine and suspension system allows the plane to perch on a rough vertical wall for a relatively large envelope of touchdown velocity and pitch angle. This envelope, computed with the simulator ($-F_n/F_s < 1$, $F_{max} < 25N$ and the knee joint not touching the wall), is illustrated in figure 11. As one can see on this figure, landing is possible not only for a zero-velocity touchdown, but for forward velocities of up to $v_x = 2.7$ m/s, pitch angles between 65 and 110 degrees and downward velocities of up to 1 m/s.

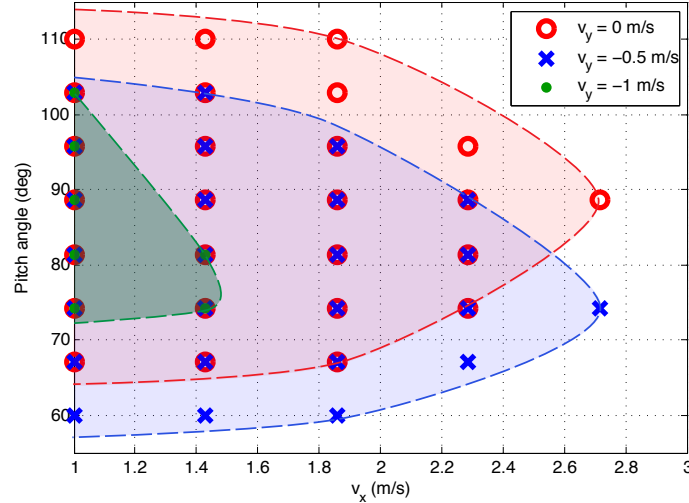


Fig. 11 Successful landings simulated for various touchdown states.

About 30 successful landings have been performed so far, out of 40 attempts, and touchdown states all over and around the limits of the computed envelope have been observed. This large envelope has numerous benefits for a small UAV system: it

reduces the requirements on the control (less need for accurate control during a short maneuver), it reduces the need for sensing (fewer, cheaper and smaller sensors), it increases the robustness of the system and it allows smooth landing at a moderate forward speed.

5 Conclusion

We have demonstrated a system in which a combination of miniature spines and a nonlinear suspension allow a small unmanned airplane to approach and land on a vertical wall. The focus of the work reported here is on the suspension design, needed to dissipate the kinetic energy of the plane while maintaining a desirable ratio of normal and tangential contact forces for spine engagement. Simulations and experiments reveal that the system accommodates a range of typical initial conditions. In practice, we have observed 30/40 successful trials in calm outdoor conditions. The models also reveal room for improvement. In particular, the damping at the proximal and especially the distal elements can be increased for a smoother progression from initial contact to steady state.

A number of immediate extensions are also warranted. The model should be enhanced to account for the dynamic effects resulting from the (stochastic) spine/wall interactions. A fully three dimensional model, with two separate legs, would also help us to explore the sensitivity to roll and yaw variations. From a practical standpoint, the short term goal is to achieve powered takeoff and resumption of flight. The ideal way to accomplish this takeoff would be to exploit stored elastic energy in the legs so as to reach controllable airspeed rapidly. In parallel, the control of the plane should be improved, with more reliable wall sensing and better control of the velocity and orientation prior to landing, particularly in the presence of wind.

Looking a bit further ahead, we recognize that we will need to deploy opposed sets of spines to resist gusts of wind after attachment. We have built opposed-spine prototypes that sustain normal forces of up to 20 N in benchtop tests and will be adapting these to the airplane. Still further ahead are developments to perform crawling maneuvers while in contact with wall, using a combination of thrust vectoring and leg motions. This will result in a true scansorial hybrid with flying and crawling behavior.

Acknowledgements Alexis Lussier Desbiens is supported by the Natural Sciences and Engineering Research Council of Canada and the Organization of American States, with additional support from DARPA DSO. We would also like to thank the members of BDML at Stanford for all their help in conducting the experiments reported here.

References

Anderson M, Perry C, Hua B, Olsen D, Parcus J, Pederson K, Jensen D (2009) The Sticky-Pad Plane and other Innovative Concepts for Perching UAVs. 47 th AIAA

Aerospace Sciences Meeting

- Asbeck A, Kim S, Cutkosky M, Provancher WR, Lanzetta M (2006) Scaling hard vertical surfaces with compliant microspine arrays. *International Journal of Robotics Research* 25(12):14
- Byrnes G, Lim NTL, Spence AJ (2008) Take-off and landing kinetics of a free-ranging gliding mammal, the malayan colugo (*Galeopterus variegatus*). *Proceedings of the Royal Society B: Biological Sciences* 275(1638):1007–1013
- Caple G, Balda RP, Willis WR (1983) The physics of leaping animals and the evolution of preflight. *The American Naturalist* 121:455–467
- Cham JG, Bailey SA, Clark JE, Full RJ, Cutkosky MR (2002) Fast and robust: Hexapedal robots via shape deposition manufacturing. *IJRR* 21(10):869–882
- Cory R, Tedrake R (2008) Experiments in fixed-wing uav perching. *Proceedings of the AIAA Guidance, Navigation, and Control Conference*
- Frank A, McGrew JS, Valenti M, Levine D, How JP (2007) Hover, transition, and level flight control design for a single-propeller indoor airplane. *AIAA Guidance, Navigation and Control Conference*
- Great Planes (2009) Electrify flatana. URL <http://www.electrify.com/flatouts/gpma1111.html>
- Green W, Oh P (2008) Autonomous hovering of a fixed-wing micro air vehicle. *IEEE International Conference of Robotics and Automation*
- Hoburg W, Tedrake R (2009) System identification of post stall aerodynamics for uav perching. *Proceedings of the AIAA Infotech@Aerospace Conference*
- Howell L (2001) *Compliant mechanisms*. Wiley-Interscience
- Jusufi A, Goldman DI, Revzen S, Full RJ (2008) Active tails enhance arboreal acrobatics in geckos. *Proceedings of the National Academy of Sciences* 105(11):4215–4219
- Kim S, Spenko M, Trujillo S, Heyneman B, Santos D, Cutkosky MR (2008) Climbing with directional adhesion. *IEEE Transactions on Robotics* 24
- Lukens J, Reich G, Sanders B (2008) Wing Mechanization Design and Analysis for a Perching Micro Air Vehicle. *49th Structures, Structural Dynamics, and Materials Conference*
- Lussier-Desbiens A, Cutkosky M (2009) Landing and Perching on Vertical Surfaces with Microspines for Small Unmanned Air Vehicles. *2nd International Symposium on Unmanned Aerial Vehicles*
- Mitiguy PC, Banerjee AK (1999) Efficient simulation of motions involving coulomb friction. *Journal of Guidance, Control and Dynamics* 22(1)
- Moore J, Tedrake R (2009) Powerline perching with a fixed-wing uav. *Proceedings of the AIAA Infotech@Aerospace Conference*
- Paparazzi (2008) Paparazzi, the free autopilot. URL <http://paparazzi.enac.fr>
- Paskins KE, Bowyer A, Megill WM, Scheibe JS (2007) Take-off and landing forces and the evolution of controlled gliding in northern flying squirrels *glaucomys sabrinus*. *Journal of Experimental Biology* 210(8):1413–1423
- Reich G, Wojnar M, Albertani R (2009) Aerodynamic Performance of a Notional Perching MAV Design. *47 th AIAA Aerospace Sciences Meeting*

- Roberts J, Cory R, Tedrake R (2009) On the controllability of fixed-wing perching. American Controls Conference
- Santos D, Kim S, Spenko M, Parness A, Cutkosky M (2007) Directional adhesive structures for controlled climbing on smooth vertical surfaces. In: IEEE ICRA, Rome, Italy
- Spenko M, Haynes G, Saunders J, Cutkosky M, Rizzi A, Full R (2008) Biologically inspired climbing with a hexapedal robot. *Journal of Field Robotics*
- Wickenheiser AM, Garcia E (2008) Optimization of perching maneuvers through vehicle morphing. *Journal of Guidance* 31(4):815–823